Article | Open Access

Micro Nano Science

Bo *et al. Micro Nano Sci.* **2026**, *1*, 11 **DOI:**10.20517/mns.2026.03

Defect engineering and machine learning enhance *n*-butanol sensing of γ-Fe_2O_3

Liang-Bo Bo#, Zhi-Lei Li#, Xiao-Hong Zheng*, Su-Yue Ren, Zi-Qi Gu, Jing-Wen Pan, Yu-Feng Liu*

Keywords:
γ-Fe_2O_3, *n*-butanol detection, oxygen vacancy engineering, machine learning correction

Citation: Bo, L. B.; Li, Z. L.; Zheng, X. H.; Ren, S. Y.; Gu, Z. Q.; Pan, J. W.; Liu, Y. F. Defect engineering and machine learning enhance *n*-butanol sensing of γ-Fe_2O_3. *Micro Nano Sci.* **2026**, *1*, 11. https://dx.doi.org/10.20517/mns.2026.03

Received: 5 Mar 2026 **First Decision:** 22 May 2026 **Revised:** 23 Jun 2026 **Accepted:** 24 Jun 2026 **Published:** 30 Jun 2026

Academic Editor: Huiling Tai
Copy Editor: Shu-Yuan Duan
Production Editor: Shu-Yuan Duan

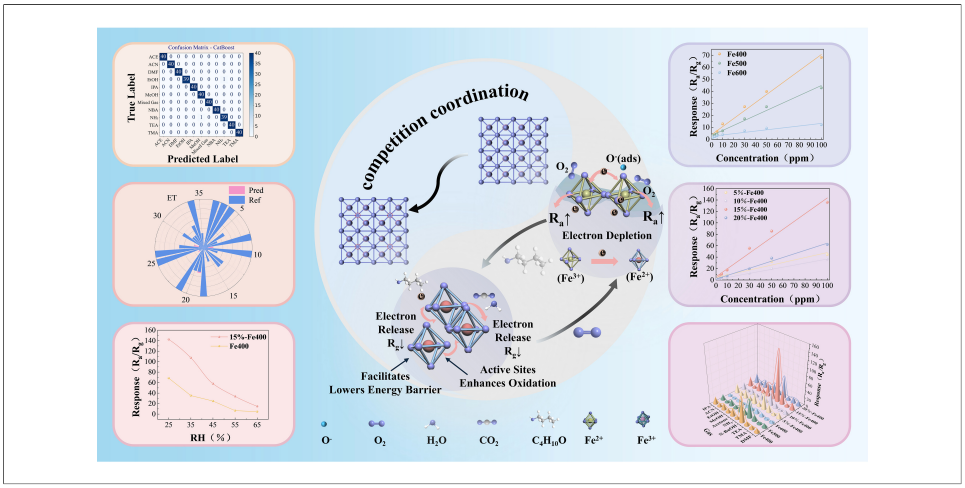

Abstract

n-Butanol, a typical volatile organic compound (VOC), is both critical and challenging to detect at trace levels in gas-sensing systems. We report a defect engineering strategy combining heat treatment with ligand-controlled coordination to synthesize maghemite (γ-Fe_2O_3) with abundant oxygen vacancies, thereby improving its sensing performance toward *n*-butanol. Introducing terephthalic acid (H_2BDC) into the MIL-100(Fe) metal-organic framework (MOF) created coordination defects that evolved into oxygen vacancies upon heat treatment at 400 °C. The Fe400 sensor exhibits a response of 66.96 to 100 ppm *n*-butanol, with response and recovery times of 53/48 s and a detection limit of 325 ppb. After optimization, the 15%-Fe400 sensor exhibits a response of 142.3 to 100 ppm *n*-butanol at 200 °C, with a detection limit of 130 ppb, outperforming most oxide-based gas sensors. The improved performance is attributed to the high oxygen vacancy concentration and γ-Fe_2O_3/Fe_3O_4 phase transformation. Additionally, machine learning models, including Extra Trees and CatBoost, were used for humidity compensation and multi-gas detection, offering a promising approach for high-performance gas sensing applications.

Faculty of Materials Technology, Shanghai Institute of Technology, Shanghai 201418, China.
#These authors contributed equally to this work.

***Correspondence to:** Xiao-Hong Zheng, Yu-Feng Liu, Faculty of Materials Technology, Shanghai Institute of Technology, Shanghai 201418, China. E-mail: zhengxiaohong@sit.edu.cn; yfliu@sit.edu.cn

INTRODUCTION

Volatile organic compounds (VOCs) are widespread pollutants in modern industry and daily life that pose serious threats to ecosystems and human health, even at trace concentrations[1]. As a typical VOC, *n*-butanol is widely used in industries such as biopharmaceutical synthesis, paint and coating production, rubber processing, and plastic manufacturing[2]. However, *n*-butanol is highly irritating and corrosive during volatilization and exposure, particularly damaging the respiratory mucosa and ocular tissues. Prolonged exposure can lead to central nervous system dysfunction, as well as skin inflammation and persistent headaches[3]. Therefore, developing high-performance *n*-butanol gas sensors with high response and selectivity, as well as low detection limits, has become a critical research focus for precise environmental monitoring and health risk control.

Metal-oxide semiconductor (MOS) gas sensors have been widely applied in environmental monitoring and safety protection owing to their low cost, fast response, and ease of integration with electronic systems[4]. However, conventional MOS sensors often exhibit poor selectivity, weak response signals, and high detection limits, which greatly limit their effectiveness in complex or humid environments. To address these limitations, various strategies have been investigated to enhance the sensitivity and selectivity of MOS sensors. Among them, metal-organic frameworks (MOFs) have garnered considerable attention due to their highly tunable structures and excellent chemical versatility[5]. By precisely controlling the composition and architecture of MOFs, metal oxide materials with adjustable pore sizes, large specific surface areas, and uniformly distributed metal species can be synthesized. This structural tunability optimizes gas adsorption and surface reaction pathways, facilitates charge transfer and redox processes, and thereby significantly improves the response and selectivity toward target gases while enabling low-temperature operation[6]. Moreover, pyrolysis of MOFs yields metal oxides with hierarchical porous architectures, providing abundant active sites for gas adsorption and catalysis. The interconnected pore network promotes efficient gas diffusion and electron transport, leading to pronounced variations in conductivity even at low gas concentrations. As a result, MOF-derived metal oxides effectively overcome the main drawbacks of traditional MOS sensors - enhancing selectivity, strengthening response intensity, and substantially lowering detection limits[7-9].

Iron-based metal-organic frameworks (Fe-MOFs) are considered ideal precursors for gas sensing due to their low cost, abundant metal sites, and high thermal stability. Upon pyrolysis, Fe-MOFs transform into porous maghemite (γ-Fe_2O_3), inheriting ordered pore channels and uniform dispersion from the precursor. The resulting material exhibits a high surface area, abundant active sites, and favorable electronic properties, thereby enhancing gas adsorption and reaction kinetics. In recent years, Fe-MOF-derived γ-Fe_2O_3 has received increasing attention in gas-sensing research. For example, Wang *et al.*[10] synthesized γ-Fe_2O_3 via solvothermal annealing, achieving a response of ~ 23-100 ppm H_2S at 90 °C. Additionally, γ-Fe_2O_3 synthesized through a two-step process has been reported to exhibit a response of 4.3 toward 100 ppm *n*-butanol at 170 °C[11]. However, the gas-sensing performance of pure-phase γ-Fe_2O_3 derived from MOFs remains limited, highlighting the need for effective modification strategies. Among various enhancement strategies, oxygen vacancy engineering has received considerable attention for its ability to increase surface reactivity and optimize electronic structure. Previous studies have validated this approach. For example, Parveen *et al.*[12] fabricated oxygen-vacancy-rich α-MoO_3 nanoribbons via copper doping, achieving an exceptional response to 100 ppm NO_2 at 170 °C. Similarly, Zhang *et al.*[13] prepared TiO_2 nanosheets with abundant oxygen vacancies through thermal decomposition, enabling efficient hydrogen detection at room temperature.

The heat-treatment temperature, as a crucial process parameter, plays a key role in determining the formation and distribution of oxygen vacancies. Paul *et al.*[14] tuned the synthesis temperature to produce $BiVO_4$ with abundant oxygen vacancies, yielding a high response of 1,421 to 270 ppm NH_3 at room

temperature. Likewise, Li *et al*.[15] precisely controlled the calcination temperature to adjust the oxygen-vacancy concentration in cubic spinel Co_3O_4, achieving a response of 42.11 to 100 ppm acetone. From a microscopic perspective, defective MOF precursors serve as ideal templates for generating oxygen vacancies due to their distinctive structural features. The intrinsic defect features of coordinatively unsaturated metal sites allow these structural imperfections to be transferred to the derived metal-oxide lattice during thermal transformation, thus facilitating the controlled formation of oxygen vacancies[16,17]. Moreover, the synergistic interplay between the thermal stability of organic ligands and the concentration of metal ions collectively governs atomic rearrangement during pyrolysis, ultimately affecting grain growth kinetics and the spatial distribution of oxygen vacancies in the resulting materials[18,19].

This study employs a defect engineering strategy that combines heat treatment with ligand-controlled coordination to enhance the gas-sensing performance of γ-Fe_2O_3. The introduction of terephthalic acid (H_2BDC) induces competition among ligands for iron ions, driven by differences in coordination affinity. Heat treatment at 400 °C converts these coordination defects into abundant oxygen vacancies. These vacancies act as active sites for gas adsorption and facilitate the reversible transformation between γ-Fe_2O_3 and Fe_3O_4. The Fe400 sensor exhibits good sensing performance toward *n*-butanol, with a response of 66.96 at 100 ppm and a detection limit of 325 ppb. Increasing the H_2BDC content further increases the oxygen vacancy concentration, thereby improving the performance of the 15% Fe400 sensor. It detects 100 ppm *n*-butanol at 200 °C with a lower detection limit of 130 ppb. Analysis indicates that high oxygen vacancy concentration and reversible phase transformation jointly enhance sensing performance. Furthermore, machine learning models were employed to reduce humidity interference. Among them, the Extra Trees model enables signal correction, while CatBoost achieves accurate gas classification. This approach provides a promising pathway for high-performance gas-sensing technologies.

EXPERIMENTAL

Chemicals

All reagents used in this study were employed as received, without further purification. Ferric chloride hexahydrate ($FeCl_3·6H_2O$, AR), 1,3,5-benzenetricarboxylic acid (H_3BTC, AR), and terephthalic acid (H_2BDC, AR) were purchased from Aladdin Reagent Co., Ltd. N, N-dimethylformamide (DMF, AR), ammonia solution ($NH_3·H_2O$, AR), triethylamine ($C_6H_{15}N$, AR), methanol (CH_4O, AR), ethanol (C_2H_6O, AR), isopropanol (C_3H_8O, AR), *n*-butanol ($C_4H_{10}O$, AR), acetone (C_3H_6O, AR), acetonitrile (C_2H_3N, AR), and trimethylamine (C_3H_9N, AR) were obtained from Sinopharm Chemical Reagent Co., Ltd. Deionized water was prepared in the laboratory.

Synthesis of Fe_2O_3 derived from defect-free MIL-100(Fe)

MIL-100(Fe) was synthesized using a hydrothermal method according to a reported procedure[20]. Briefly, $FeCl_3·6H_2O$ (4 mM) and H_3BTC (4 mM) were dissolved in 80 mL of DMF by ultrasonic agitation for 30 min. The solution was transferred to a 100 mL Teflon-lined autoclave and heated at 150°C for 12 h. After cooling to room temperature, the product was sequentially washed with DMF and anhydrous ethanol and then dried to obtain MIL-100(Fe). The synthesized MIL-100(Fe) was thermally treated for 12 h in a ceramic crucible under a nitrogen atmosphere at temperatures ranging from 200 to 600 °C. The resulting products were designated as Fe_x (x = 200, 300, 400, 500, and 600), where x represents the heat-treatment temperature. The synthesis process is illustrated in Supplementary Figure 1.

Synthesis of defect-rich MIL-100(Fe)-derived γ-Fe_2O_3

In the preparation of MIL-100(Fe), different amounts of terephthalic acid were added (5 mol.% H_2BDC, 10 mol.% H_2BDC, 15 mol.% H_2BDC, and 20 mol.% H_2BDC). The mixture was subjected to ultrasonic treatment followed by a hydrothermal reaction. After the reaction, the products were cooled to room temperature, sequentially washed with DMF and ethanol, and then dried. The synthesized powder was then heated at 400 °C for 12 h under a nitrogen atmosphere. The resulting samples were named x%-Fe400 (where x = 5, 10, 15, and 20). The synthesis flowchart is shown in Supplementary Figure 1.

Characterization

Powder X-ray diffraction (XRD) patterns were recorded on a TD-3500 X-ray diffractometer (Dandong Tongda Science & Technology Co., Ltd., China) using Cu Kα radiation (λ = 1.54056 Å) over a 2θ range of 10-80° at a scanning rate of 6° min^{-1} to investigate the phase composition and crystal structure of the samples. The surface morphology was observed by scanning electron microscopy (SEM, ZEISS Gemini Sigma 300, Germany). Transmission electron microscopy (TEM) and high-resolution transmission electron microscopy (HRTEM) analyses were performed on an FEI Talos F200S microscope to examine the microstructure and crystalline features of the materials. Elemental mapping was conducted simultaneously during TEM characterization to analyze the elemental distribution on the sample surface. X-ray photoelectron spectroscopy (XPS) was performed using an ESCALAB 250Xi+ spectrometer (Thermo Fisher Scientific, USA) to determine the elemental composition and chemical states of the samples. Nitrogen adsorption-desorption measurements were performed on an ASAP 2020 automatic physisorption analyzer (Micromeritics, USA) to determine the specific surface area and pore-size distribution. The specific surface area was calculated using the Brunauer-Emmett-Teller (BET) method, and the pore size distribution was obtained from the desorption branch based on the Barrett-Joyner-Halenda (BJH) method. Thermogravimetric analysis (TGA) was conducted on an SDT Q600 thermal analyzer (TA Instruments, USA) under a nitrogen atmosphere at a heating rate of 5 °C min^{-1} to evaluate the thermal stability of MIL-100(Fe). Electron paramagnetic resonance (EPR) spectroscopy was performed on a Bruker EMXplus-6/1 spectrometer (Bruker, Germany) to analyze oxygen vacancy defects. Raman spectra were collected using a HORIBA LabRAM Odyssey spectrometer (Japan) with 532 nm excitation to probe molecular structure and chemical bonding. UV-vis absorption spectra were measured using a Cary 5,000 UV-vis spectrophotometer (Agilent, USA) in the wavelength range of 300-800 nm to estimate the band gap. Photoluminescence (PL) spectra were obtained using an F-7000 fluorescence spectrophotometer (Hitachi, Japan) to evaluate the defect-related emission characteristics of the materials.

Sensor fabrication and sensing measurement

A homogeneous paste was prepared by uniformly dispersing 0.02 g of MIL-100(Fe)-derived γ-Fe_2O_3 sensing material in 15 μL of ethanol, followed by coating the paste onto ceramic tubes (1.2 mm OD (outer diameter), 0.8 mm ID (inner diameter), and 4 mm length). Each tube incorporated gold electrodes at both ends, which were connected to platinum wires. A Ni-Cr alloy heating wire inserted into an alumina tube enabled precise temperature control via regulated voltage application. To enhance stability, all sensors were aged at 240 °C for 48 h in ambient air.

Gas-sensing performance was evaluated using a WS-30B system (Weisheng Instruments Co., Ltd.). The operating temperature was controlled by adjusting the heating wire voltage, while relative humidity (RH) was regulated through controlled water evaporation prior to testing. All measurements were performed under standard conditions (25% ± 5% RH, 23 ± 2 °C) unless otherwise noted.

The sensor resistances in air and target gas are denoted as R_a and R_g, respectively. For n-type semiconductors in a reducing atmosphere, the response (R_{es}) is defined as R_a/R_g. The response time (T_{res}) and recovery time

(T_{rec}) are defined as the time to reach 90% of the total resistance change upon gas exposure and air recovery, respectively. Sensitivity is defined as the reciprocal of the slope of the sensor's calibration curve. The concentration of volatile organic compounds generated by thermal evaporation was calculated using[21]:

$$C(\text{ppm}) = \frac{V_x(\text{ mL}) \times P \times \rho(\text{g/mL}) \times 22.4(\text{ L/mol})}{M(\text{ g/mol}) \times V(\text{ L})} \times 10^6 \quad (1)$$

where C is the gas concentration (ppm), V_x is the liquid volume (mL), P is the purity (fraction), ρ is the density (g/mL), M is the molecular weight (g/mol), and V is the chamber volume (18 L). In practice, the liquid samples were precisely measured and introduced into the evaporation platform using a microsyringe.

RESULTS AND DISCUSSION

Structural characterization

The TGA of MIL-100(Fe) reveals a multistage thermal decomposition process, as shown in Supplementary Figure 2. In the first stage (25-138 °C), the material loses 35.76% of its weight due to the removal of adsorbed and crystalline water. This stage does not damage the framework but prepares it for further degradation[22]. The second stage (138-426 °C) involves a 25.7% weight loss[23], primarily due to the removal of terminal unbridged anionic ligands and partial degradation of the organic framework, marking the onset of framework breakdown. In the third stage (426-455 °C)[24], a further weight loss of 13.68% occurs as the framework undergoes more significant decomposition. The fourth stage (455-560 °C) shows a 10.24% weight loss, indicating continued degradation and eventual collapse of the framework as the remaining organic components decompose. Based on the TGA results, further processing was carried out at heat treatment temperatures of 200, 300, 400, 500, and 600 °C.

Phase analysis was conducted using XRD patterns of all samples. As shown in Supplementary Figure 3A, Fe200 and Fe300 showed no characteristic diffraction peaks corresponding to Fe_2O_3. As the temperature increased, the diffraction peaks of Fe400 and Fe500 were indexed to γ-Fe_2O_3 (JCPDS No. 39-1346)[25], whereas those of Fe600 corresponded to α-Fe_2O_3 (JCPDS No. 33-0664)[26], indicating a phase transition from a metastable to a stable iron oxide phase. Maghemite (γ-Fe_2O_3) is a metastable polymorph of iron(III) oxide that gradually transforms into the thermodynamically stable hematite (α-Fe_2O_3) phase upon thermal treatment. Under ambient conditions, α- Fe_2O_3 is the most stable Fe_2O_3 polymorph, whereas γ-Fe_2O_3 can transform into α-Fe_2O_3 at elevated temperatures, typically within several hundred degrees Celsius, depending on the synthesis method and particle size[27,28]. As shown in Supplementary Figure 3B, the sample still retains the γ-Fe_2O_3 phase after introducing H_2BDC, with sharper diffraction peaks. Combined with the data in Supplementary Table 1, this further confirms that the addition of H_2BDC significantly enhances phase purity and crystallinity. Scherrer equation analysis [Supplementary Table 2] shows that the crystallite size increases progressively with higher ligand concentrations. Overall, the XRD results highlight a strong synergistic effect between thermal treatment and chemical modulation: temperature governs phase evolution[29], while an optimal concentration of H_2BDC enhances crystallinity and promotes crystal growth.

As shown in Figure 1A, the MIL-100 sample thermally treated at 400 °C under an N_2 atmosphere exhibits a composite morphology consisting of stacked octahedra and irregular nanoparticles. This is attributed to the synergistic effect of the "morphological inheritance" and "decomposition-recrystallization" mechanisms during the heat treatment process[30,31]. As further shown in Supplementary Figure 4A and B, with increasing heat treatment temperature, the framework gradually decomposes at 500 and 600 °C, accompanied by localized structural collapse and significant sintering-induced agglomeration. This structural evolution is

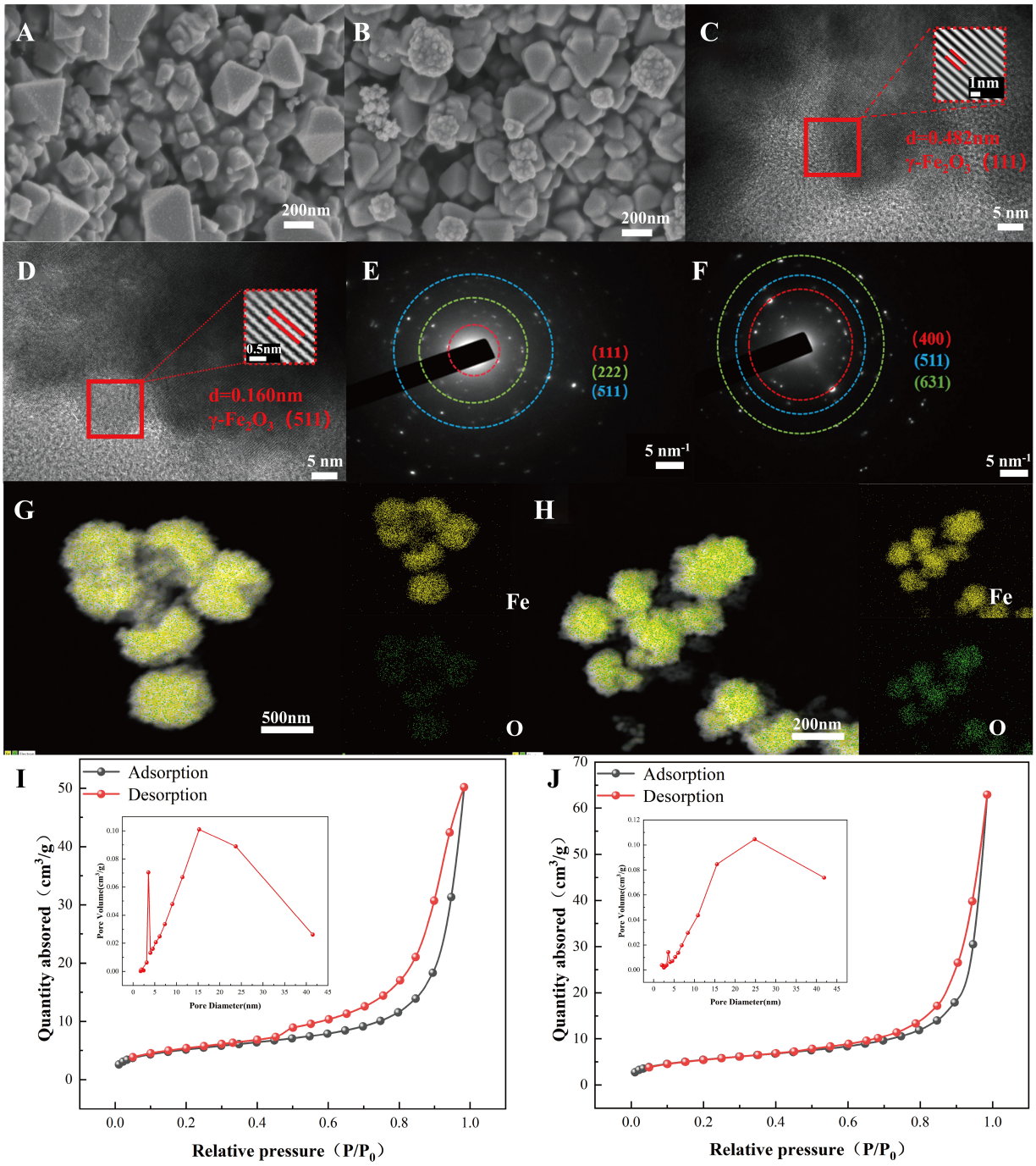

Figure 1. (A and B) SEM images of Fe400 and 15%-Fe400; (C and D) HRTEM images of Fe400 and 15%-Fe400; (E and F) SAED patterns of Fe400 and 15%-Fe400; (G and H) EDS elemental mapping of Fe and O in Fe400 and 15%-Fe400 samples; The BET specific surface area and pore-size distribution of Fe400 and 15%-Fe400 are shown in panels (I and J), respectively. All subfigures are original. Panels (A and D) were directly exported from the SEM instrument; panels (B, C, E and F) were directly exported from the TEM instrument; panels (G and H) were directly exported from the EDS mapping system; panels (I and J) were plotted using Origin 2024. SEM: Scanning electron microscopy; HRTEM: high-resolution transmission electron microscopy; EDS: energy-dispersive X-ray spectroscopy; SAED: selected-area electron diffraction; BET: Brunauer-Emmett-Teller; TEM: transmission electron microscopy.

consistent with the TGA results. SEM images in Figure 1B and Supplementary Figure 4C-E reveal that as the H_2BDC content increases, the Fe_2O_3 particle size progressively increases, indicating a pronounced size-tuning effect consistent with the XRD results. Meanwhile, the morphology changes accordingly, likely due to additional framework decomposition induced by the higher ligand concentration.

The microstructure and elemental composition of the Fe400 and 15%-Fe400 samples were systematically characterized using TEM. The corresponding magnified TEM images and HRTEM insets [Figure 1C and D] reveal well-defined lattice fringes, with measured interplanar spacings closely matching the characteristic planes of γ-Fe_2O_3, thereby confirming the phase composition of the samples. This result is consistent with the XRD analysis discussed earlier. The selected-area electron diffraction (SAED) patterns [Figure 1E and F] display sharp polycrystalline rings, indicating that both samples possess a typical polycrystalline structure[32]. The energy-dispersive X-ray spectroscopy (EDS) elemental mapping results [Figure 1G and H] show a uniform spatial distribution of Fe and O in both samples. Notably, the oxygen signal is markedly stronger in the 15%-Fe400 sample.

Figure 1I and J presents the nitrogen adsorption-desorption isotherms and corresponding pore-size distributions of the Fe400 and 15%-Fe400 samples. According to IUPAC classification[33], both samples exhibit type IV isotherms with H3-type hysteresis loops, confirming the successful formation of a porous structure through thermal treatment of the MIL-100(Fe) precursor. Although such porous structures can provide transport pathways for gas adsorption and diffusion, the BET specific surface areas of Fe400 and 15%-Fe400 are 18.81 and 19.87 $m^2 g^{-1}$, respectively, showing only a slight difference.

According to the EDS results [Figure 2A and B], the Fe:O atomic ratio changes from 1.8:1 for Fe400 to 1.8:2.16 for 15%-Fe400, indicating an increase in oxygen content after modification. This oxygen enrichment is mainly attributed to structural and chemical changes induced by the addition of 15% H_2BDC to the precursor. Specifically, the incorporation of H_2BDC optimizes the coordination environment of the metal centers and promotes the formation of structural defects within the framework. During subsequent heat treatment, these defects evolve into oxygen vacancies, which enhance oxygen adsorption and retention. As a result, the H_2BDC-modified sample shows a significantly higher oxygen content than the unmodified Fe400, highlighting the important role of organic ligand modulation in controlling oxygen distribution during thermal processing.

Figure 2C-G presents the XPS survey spectra as well as the Fe 2p and O 1s spectra of Fe400 and 15%-Fe400, while the corresponding spectra of the other samples are shown in Supplementary Figure 5. The survey spectra [Figure 2C] show clear signals from Fe, O, and C, with no detectable impurities, confirming the high phase purity of γ-Fe_2O_3 and consistent with the XRD results. Gaussian fitting of the Fe 2p spectra [Figure 2D and E] reveals peaks at 710.4 eV and 724.0 eV, assigned to Fe $2p_{3/2}$ and Fe $2p_{1/2}$, respectively, which are characteristic of Fe^{3+} species[34]. The O 1s spectra [Figure 2F-I] can be deconvoluted into three components corresponding to lattice oxygen (O_L), oxygen vacancies (O_V), and chemisorbed oxygen (O_C). Among all samples, Fe400 and 15%-Fe400 show the highest oxygen-vacancy concentrations, while EDS confirms that 15%-Fe400 has the highest overall oxygen content. These results indicate that introducing H_2BDC into the precursor promotes the formation and stabilization of oxygen vacancies during heat treatment. The increased concentration of oxygen vacancies enhances gas adsorption, facilitates charge transfer, and improves surface reactivity, thereby contributing to the superior gas-sensing performance of 15%-Fe400.

As shown in Figure 2J, the Raman spectra of Fe400 and 15%-Fe400 exhibit distinct differences in vibrational behavior. The 15%-Fe400 sample shows broader and weaker peaks than Fe400, indicating a higher degree of structural disorder and a higher defect density. Such peak broadening and intensity reduction are typically associated with oxygen vacancies and lattice distortions in γ-Fe_2O_3 structures[35]. The addition of H_2BDC likely modifies the local coordination environment of Fe atoms, promoting oxygen vacancy formation during thermal treatment.

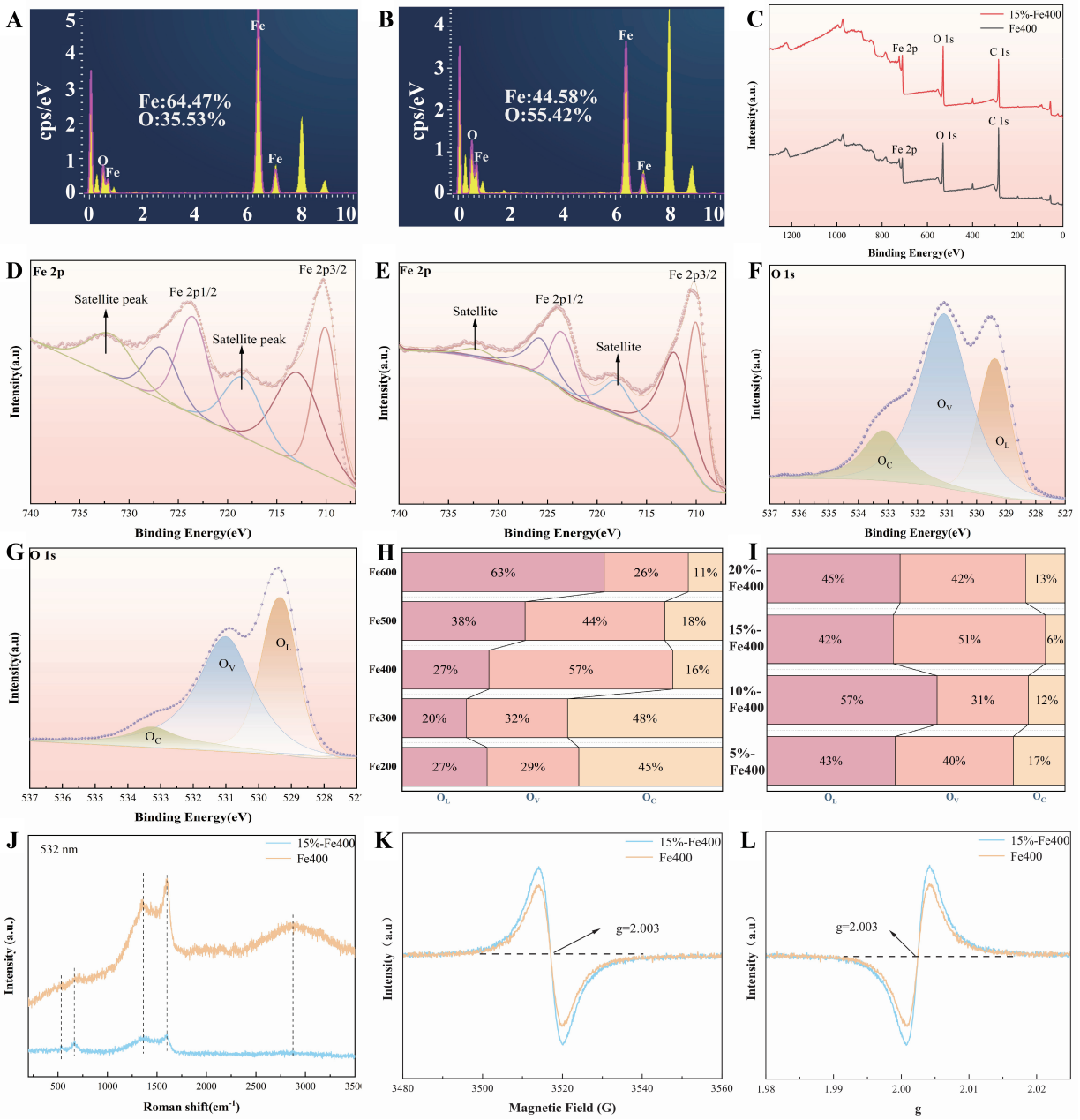

Figure 2. (A) EDS spectrum of Fe400; (B) EDS spectrum of 15%-Fe400; (C) XPS survey spectra of Fe400 and 15%-Fe400; (D) High-resolution Fe 2p XPS spectrum of Fe400; (E) High-resolution Fe 2p XPS spectrum of 15%-Fe400; (F) High-resolution O 1s XPS spectrum of Fe400; (G) High-resolution O 1s XPS spectrum of 15%-Fe400; (H) The distribution of oxygen elements in the samples after heat treatment at different temperatures; (I) Oxygen species distribution in samples with different additive ratios; (J) Raman spectra of 15%-Fe400 and Fe400; (K) Magnetic field-swept EPR spectra of Fe400 and 15%-Fe400; (L) Corresponding g-factor spectra of Fe400 and 15%-Fe400. All subfigures are original. Panels (A and B) were directly exported from the EDS characterization system; panels (C-L) were plotted using Origin 2024. EDS: Energy-dispersive X-ray spectroscopy; XPS: X-ray photoelectron spectroscopy; EPR: electron paramagnetic resonance; RH: relative humidity.

To further confirm these findings, EPR spectroscopy was used to probe unpaired electrons associated with oxygen-deficient sites [Figure 2K and L]. As shown in Figure 2K, the magnetic field-swept EPR spectra of 15%-Fe400 exhibit a significantly stronger signal than Fe400, indicating a higher concentration of paramagnetic centers. In the corresponding g-factor plots [Figure 2L], both samples exhibit resonance peaks at g 2.003, characteristic of oxygen-vacancy-related centers[36]. The much stronger signal at this g value for 15%-Fe400 further confirms its higher oxygen-vacancy concentration. Together, the EPR and Raman results

provide strong evidence that H_2BDC modification promotes the formation and stabilization of oxygen vacancies. This increased vacancy concentration enhances surface reactivity and charge-transfer capability, thereby improving the gas-sensing performance of 15%-Fe400.

Gas-sensing performance

To evaluate the gas-sensing performance of MIL-100(Fe)-derived materials, their fundamental sensing properties were systematically studied. As shown in Supplementary Figure 6A, the responses of samples treated at different temperatures toward 100 ppm *n*-butanol were compared. Fe200 and Fe300 showed negligible responses and were therefore excluded from further analysis. Based on the structural characterization, this weak response is mainly attributed to the incomplete conversion of the MIL-100(Fe) precursor into crystalline Fe_2O_3 at relatively low treatment temperatures. Such insufficient phase transformation leads to a poorly crystallized or partially decomposed structure, which is unfavorable for forming continuous electron-transport pathways within the sensing layer[37]. In addition, the limited formation of crystalline γ-Fe_2O_3 reduces the number of effective surface sites for oxygen adsorption and activation, thereby weakening the interaction between adsorbed oxygen species and *n*-butanol molecules[38]. Consequently, the charge-transfer process is inhibited, leading to an almost undetectable response of Fe200 and Fe300 to *n*-butanol.

Figure 3A shows that the responses of all sensors to 100 ppm *n*-butanol follow a characteristic volcano-shaped trend with increasing operating temperature. The operating temperature influences sensing performance by controlling the balance between adsorption, activation, and desorption of gas molecules. At lower temperatures, molecular activation is insufficient, whereas at higher temperatures, desorption dominates[39]. The results show that the optimal operating temperature for the 15%-Fe400 sensor is 200 °C, which is significantly lower than the 250 °C required for the other sensors. At this temperature, the 15%-Fe400 sensor achieves a response of 142.3, which is more than 2.13 times higher than that of the other sensors. This improved performance is attributed to the higher oxygen-vacancy concentration, well-developed porous structure, and larger specific surface area of the 15%-Fe400 material.

Supplementary Figure 6B and C shows the dynamic response-recovery behavior of the sensors toward 1-100 ppm *n*-butanol under the same conditions. The sensor response increases with increasing gas concentration and quickly returns to baseline upon exposure to air. As shown in Figure 3B and C, the responses exhibit a strong linear relationship with concentration across the tested range, indicating suitability for quantitative detection over a wide concentration range. Using the theoretical detection limit equation (3×RMSnoise/slope)[40], the Fe400 sensor shows a detection limit of 325 ppb for *n*-butanol, which is significantly lower than that of the other samples. Although the 15%-Fe400 sensor shows slightly reduced linear fitting accuracy (R^2 = 0.981) at higher concentrations due to its stronger response, it achieves a theoretical detection limit of 130 ppb, the lowest among all samples, demonstrating excellent potential for trace-level detection. Table 1 summarizes the linear-fitting equations and corresponding limits of detection (LOD) for different sensors at their optimal operating temperatures. Notably, at 200 °C, the 15%-Fe400 sensor exhibits the lowest detection limit, highlighting its superior sensitivity and quantitative capability.

Figure 3D shows that all sensors rapidly return to baseline after gas switching, with minimal fluctuations and excellent repeatability, indicating stable operation. Selectivity tests [Figure 3E] show that all sensors exhibit good selectivity toward *n*-butanol, with the 15%-Fe400 sensor showing the best performance. Its response to *n*-butanol is approximately 12.1, 6.4, 5.6, and 3.6 times higher than those to methanol, ethanol, isopropanol, and triethylamine, respectively, confirming excellent selectivity. In addition, responses to alcohols increase with increasing carbon chain length, attributed to additional -CH_2- groups that promote surface dehydrogenation reactions and enhance sensing performance[41].

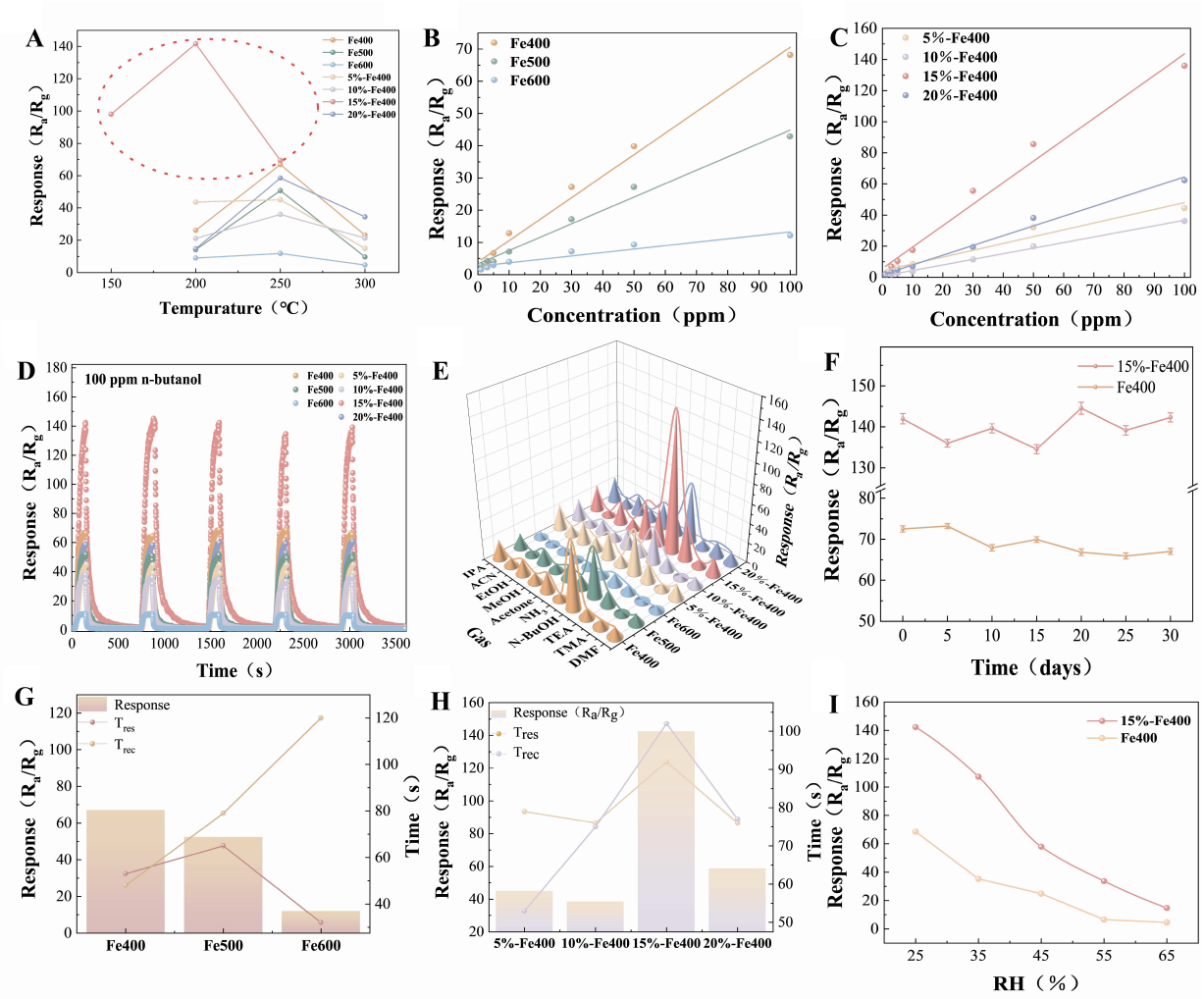

Figure 3. (A) Response to 100 ppm *n*-butanol at different operating temperatures; (B and C) Linear fitting of response-concentration data from Supplementary Figure 6B and C; (D) Cyclic response to 100 ppm *n*-butanol; (E) Selectivity toward 100 ppm various VOCs; (F) 30-day stability of Fe400 and 15%-Fe400 sensors to 100 ppm *n*-butanol. Error bars denote the standard error of the mean (SEM) from 35 independent measurements; (G and H) Response/recovery times and response values to 100 ppm *n*-butanol for sensors subjected to heat treatment at different temperatures and with various H_2BDC contents; (I) Responses of Fe400 and 15%-Fe400 sensors to 100 ppm *n*-butanol under different relative humidities. All subfigures are original. Panels (A-I) were plotted using Origin 2024. VOC: Volatile organic compound; H_2BDC: terephthalic acid.

Table 1. Linear fitting equations and LOD for different sensors at their optimal operating temperatures

Sensing materials	Linear fitting equation	Operating temperature (°C)	R^2	LOD (ppb)
Fe400	$Y = 3.88454 + 0.66684 \times X$	250	0.98768	325
Fe500	$Y = 3.21513 + 0.41559 \times X$	250	0.98686	521
Fe600	$Y = 2.58482 + 0.10673 \times X$	250	0.9297	899
5%-Fe400	$Y = 4.21467 + 0.4383 \times X$	250	0.9605	358
10%-Fe400	$Y = 0.76924 + 0.35921 \times X$	250	0.99806	429
15%-Fe400	$Y = 5.63663 + 1.37955 \times X$	200	0.981	130
20%-Fe400	$Y = 1.63778 + 0.62822 \times X$	250	0.98937	289

LOD: Limits of detection; R^2: coefficient of determination.

Long-term stability tests [Figure 3F] show that the sensor response variation remains within ±10% over 30 days, confirming excellent durability. All data are presented as mean ± standard error of the mean from 35

Table 2. Comparison of *n*-butanol sensors based on various metal oxides

Sensing material	Operating temperature (°C)	Concentration (ppm)	T_{res}/T_{rec}(s)	R_a/R_g	D_L (ppm)	Ref.
ZnO	240	100	222/26	32.4	-	[44]
$ZnSnO_3$- 2	275	100	99/52	40.5	0.5	[45]
$ZnO/CuCo_2O_4$	240	100	45/79	78.1	5	[46]
$FeVO_4$ nanofibers (550)	300	100	3/14	4.1	8.6	[47]
Co-doped $BiVO_4$	300	100	149/38	51.8	0.085	[48]
NiO/Fe_2O_3	200	100	120/64	24.2	0.048	[49]
Discoid Bi_2WO_6@α-Fe_2O_3	260	50	8/540	22.8	0.083	[50]
4 at% Ni-Bi_2WO_6	325	100	75/3	50.2	0.53	[51]
Fe400	250	100	53/48	66.96	0.325	This work
15%-Fe400	200	100	92/102	142.3	0.13	This work

independent measurements, and error bars represent the standard error of the mean. Figure 3G compares the response, response time, and recovery time of unmodified heat-treated samples Fe400, Fe500, and Fe600. Among them, Fe400 shows the best overall sensing performance, with fast response and recovery times (T_{res} = 53 s, T_{rec} = 48 s) and a high response (R_{es} = 66.96).

Figure 3H presents the response times and recovery times of sensors prepared with different H_2BDC loadings. Although the 15%-Fe400 sensor achieves the highest response (R_{es} = 142.3), it exhibits longer response and recovery times (T_{res} = 92 s, T_{rec} = 102 s). This is attributed to its higher response magnitude, which requires more extensive gas desorption, and to the relatively low operating temperature, which slows the desorption process[42]. Detailed response-recovery profiles are shown in Supplementary Figure 6D and E.

To evaluate environmental applicability, the responses of Fe400 and 15%-Fe400 to *n*-butanol were measured under different RH levels [Figure 3I]. With increasing humidity, both sensors show an approximately linear decrease in response. This is mainly due to competitive adsorption of water molecules on active sites, which occupy oxygen adsorption sites, inhibit oxygen activation, and weaken the charge-transfer reaction between *n*-butanol chemisorbed oxygen species, thereby reducing the effective sensitivity of the sensing layer[43]. Table 2 compares the sensing performance of the sensors developed in this work with previously reported materials. The Fe400 sensor shows fast response and recovery, while the 15%-Fe400 sensor exhibits a higher response and lower detection limit, confirming its enhanced sensitivity and improved sensing performance.

Machine learning

Gas sensors operating for extended periods in complex environments often experience performance degradation due to fluctuations in ambient temperature and humidity. Prolonged exposure of the sensing layer to such varying conditions can lead to baseline drift and signal distortion, thereby reducing detection accuracy and long-term stability[52]. Among these factors, humidity has the greatest impact because adsorbed water molecules compete for active sites and alter charge-transfer pathways, leading to systematic measurement errors.

As shown in Figure 3I, the 15%-Fe400 sensor exhibits clear humidity-dependent deviations, highlighting the need for compensation. To visualize this effect, a ring-stacked chart was used to compare the daily measured concentration (Conc) with the reference value (Ref) obtained from the linear fitting equation [Supplementary Figure 7A]. In this chart, the pink and blue regions represent Conc and Ref, respectively. The degree of overlap between these regions intuitively reflects measurement consistency - greater overlap

indicates closer agreement between sensor readings and reference values, implying higher reliability. This visualization effectively captures day-to-day variations in measurement deviation and provides a straightforward way to assess long-term stability.

To correct humidity-induced signal drift, a machine learning-based calibration framework was developed using 35 days of continuous monitoring data collected under varying humidity conditions. The raw response data, along with temperature and relative humidity, were used as model inputs. A total of 35 datasets were randomly split into training and test sets at an 8:2 ratio [Supplementary Table 2]. The 15%-Fe400 sensor, selected for its strong response amplitude, exhibited distinct signal variation, resulting in more reliable calibration results.

This study first applied linear regression (LR) for single-variable calibration[53]. As shown in Supplementary Figure 7B, LR slightly improved accuracy; however, its correction capability remained limited under complex conditions because it cannot capture the coupled effects of temperature and humidity. To address this limitation, a multidimensional calibration framework was developed by incorporating temperature and humidity as additional input features. Four machine learning algorithms - neural network (NN), decision tree (DT), random forest (RF), and extra trees (ET) - were used for nonlinear modeling. The NN model consisted of two hidden layers with 64 neurons each using rectified linear unit (ReLU) activation, followed by a linear output layer. For tree-based models, the DT model was implemented without a predefined maximum depth; the RF model used 100 trees with unrestricted depth; and the ET model used 50 trees with no maximum depth, a minimum split size of 6 samples, a minimum leaf size of 2 samples, and all features considered at each split.

All four models significantly improved prediction accuracy. Among them, the ET-based model achieved the best performance, with predicted concentrations closely matching reference values [Figure 4A and Supplementary Figure 7C-E]. Cumulative distribution function (CDF) analysis further confirmed that the ET model reached 100% cumulative probability at an error threshold of 0.28, outperforming conventional methods [Figure 4B]. In the target plot [Figure 4C], the ET model point lies closest to the origin, indicating minimal deviation and superior accuracy[54]. The quantitative comparison [Table 3] further shows that the ET model achieves the lowest mean squared error (MSE) and the highest coefficient of determination (R^2), confirming its strong accuracy and generalization for humidity correction.

When applied to other sensors [Supplementary Figure 7F-H], the correction model produced outputs that were highly consistent with the reference values, confirming its strong generalizability and practical applicability. The corresponding raw data are listed in Supplementary Tables 3-5. After correction using the ET model, the R^2 for the 5%-Fe400, 10%-Fe400, 15%-Fe400, and 20%-Fe400 sensors were 0.9628, 0.9677, 0.9793, and 0.8734, respectively. Among them, the 15%-Fe400 sensor exhibited the highest fitting accuracy, mainly due to its higher oxygen vacancy concentration (as shown in Supplementary Figure 6A). The increased oxygen vacancies provide more active adsorption sites, leading to a more balanced competition between gas molecules and water vapor. Consequently, this sensor shows a more stable response and the smallest calibration error under varying humidity conditions.

Building on the drift correction approach discussed above, additional experiments were conducted to evaluate the sensors' multi-gas recognition capability. Four sensors - 5%-Fe400, 10%-Fe400, 15%-Fe400, and 20%-Fe400 - were tested for the detection of ten single-component gases and one mixed gas, each at a concentration of 100 ppm [Figure 4D and Supplementary Figure 7I-K]. Each gas was sampled continuously for 200 s at 1 Hz, yielding a total of 2,200 feature datasets. The corrected signals were used as input features, and the dataset was split into training and testing sets in an 8:2 ratio. To further evaluate model robustness,

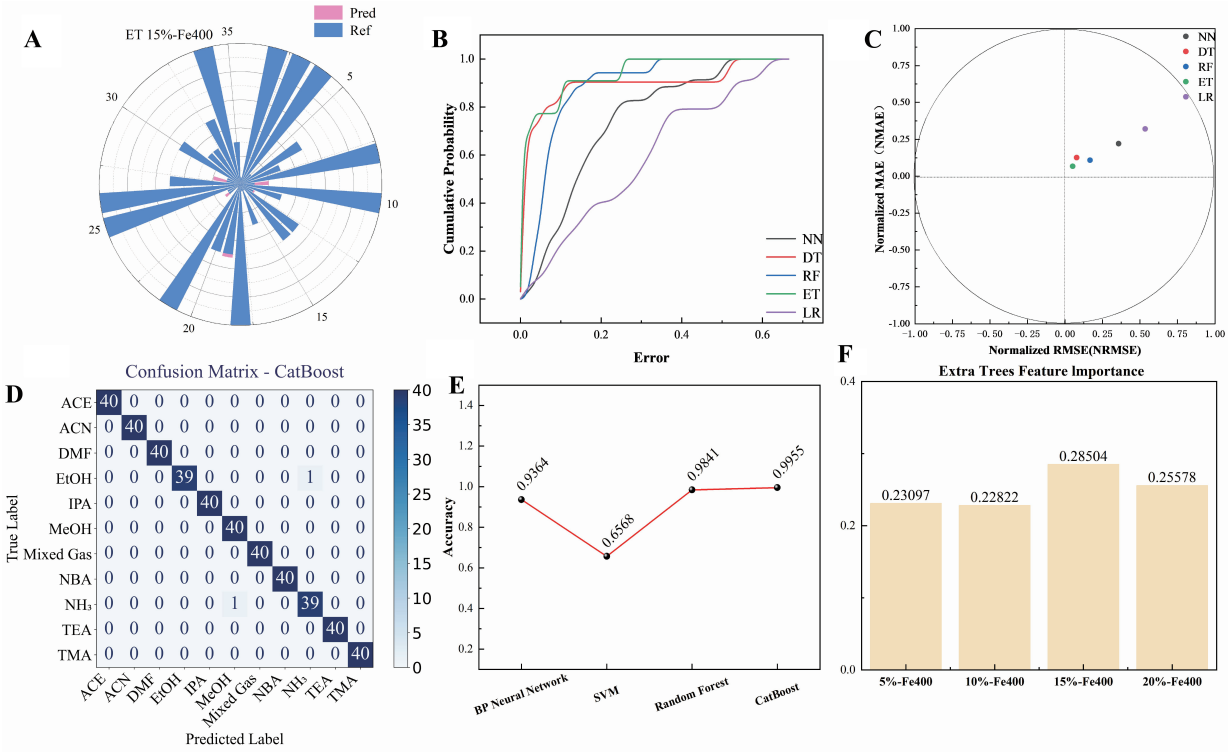

Figure 4. (A) Corrected concentration using extra trees (ETs); (B) Empirical cumulative distribution function of calibration errors; (C) Target Plot of ML Models; (D) Confusion matrix heatmaps for gas classification using four sensors, corresponding to the CatBoost algorithm; (E) Accuracy plot of the algorithms; (F) Feature analysis plot for the four sensors. All subfigures are original. Panels (A), (B), (C), (E), and (F) were plotted using Origin 2024. Panel (D) was plotted using Python/matplotlib. NN: Neural network; DT: decision tree; RF: random forest; ET: extra tree; LR: linear regression; RMSE: root mean square error; ACE: acetone; ACN: acetonitrile; DMF: N, N-dimethylformamide; IPA: isopropyl alcohol; NBA: n-butanol; TEA: triethylamine; TMA: trimethylamine; BP: Backpropagation; SVM: Support Vector Machine; ML: machine learning.

Table 3. Average performance of machine learning algorithm validation

Algorithm	MAE	RMSE	R^2	PCC
LR	18.3285	23.9203	0.2742	0.5368
NN	12.0441	14.8305	0.6567	0.8148
DT	15.7142	26.8594	0.8876	0.9460
RF	14.45571	18.6084	0.9163	0.9659
ET	10.0209	12.7134	0.9793	0.9849

MAE: Mean absolute error; RMSE: root mean square error; PCC: pearson correlation coefficient; LR: linear regression; NN: neural network; DT: decision tree; RF: random forest; ET: extra tree; R^2: coefficient of determination.

stratified five-fold cross-validation was performed for the best-performing classification model. Four machine learning algorithms, including Backpropagation Neural Network (BPNN), Support Vector Machine (SVM), Random Forest (RF), and CatBoost, were employed for classification and identification. The BPNN contained one hidden layer with 100 neurons and was trained with a maximum of 1,000 iterations. The RF classifier used 100 trees without a predefined maximum depth. The CatBoost classifier was trained using 700 boosting iterations, a learning rate of 0.1, a tree depth of 10, an L2 leaf regularization coefficient of 5, a border count of 64, a bagging temperature of 1, and a random strength of 5. The results showed that the CatBoost model achieved the highest recognition accuracy on the test set (99.55%, Figure 4E) due to its gradient-boosting mechanism and ability to handle complex nonlinear gas-response data[55].To further evaluate model robustness and check for overfitting, leave-one-out cross-validation (LOOCV) was performed on the

optimized Extra Trees model. As shown in Supplementary Figure 8A, the LOOCV root mean square error (RMSE) is 1.89 times that of the training set, indicating that the validation error remains within an acceptable range. Supplementary Figure 8B presents the five-fold cross-validation outcomes of the CatBoost classifier. The results show stable performance across all folds, further confirming that this classification model is not overfitted.

Feature analysis plot [Figure 4F] revealed that the 15%-Fe400 sensor contributed most significantly to gas discrimination. This is attributed to its optimized iron-doping ratio and oxygen vacancy concentration, which not only maintain a high carrier concentration but also create abundant active adsorption sites. As a result, response differences among different gas molecules are amplified, enhancing both sensitivity and discrimination. In summary, machine learning not only improved humidity-drift correction of the gas sensors but also provided high-quality input features for multi-gas selectivity analysis. By combining ET-based calibration with CatBoost-based recognition, this study introduces a "correct-then-identify" strategy that offers a promising approach for developing intelligent, environmentally adaptive gas-sensing systems.

Gas-sensing mechanism

Conventional MOS gas sensors detect target gases by monitoring changes in the sensing material's resistance during adsorption and desorption. When the sensor is exposed to air, oxygen molecules adsorb on the material surface and capture electrons from the conduction band, forming chemisorbed oxygen species such as O_2^-, O^-, and O^{2-}(as shown in the equations below)[56]. The sensors developed in this work exhibit an optimal operating temperature range of 100-300 °C, within which O^- is the dominant adsorbed oxygen species.

$$O_2(\text{gas}) \rightarrow O_2(\text{ads}) \tag{2}$$

$$O_2(\text{ads}) + e^- \rightarrow O_2^-(\text{ads})\ (T \leq 100^\circ C) \tag{3}$$

$$\text{ads}) + e^- \rightarrow 2O^-(\text{ads})\ (100^\circ C < T < 300^\circ C) \tag{4}$$

$$^-(\text{ads}) + e^- \rightarrow O^{2-}(\text{ads})\ (T \geq 300^\circ C) \tag{5}$$

Unlike conventional MOS sensing materials, whose resistance modulation mainly depends on changes in the surface depletion layer width, the resistance variation in γ-Fe_2O_3 is primarily attributed to a reversible phase transition between a "defective spinel" (metastable state) and a "perfect spinel" (stable state), driven by the Fe^{3+}/Fe^{2+} valence change in the lattice. This process enables chemiresistive gas sensing. γ-Fe_2O_3 has a typical defective spinel structure with octahedral Fe vacancies, whereas Fe_3O_4 possesses an inverse spinel structure containing mixed-valence Fe^{2+}/Fe^{3+} species. Previous studies have shown that iron oxides can undergo reversible phase evolution under reducing and oxidizing atmospheres. Specifically, γ-Fe_2O_3 can be partially reduced to Fe_3O_4 through the conversion of Fe^{3+} to Fe^{2+}, while Fe_3O_4 can be reoxidized to γ-Fe_2O_3 in oxygen-containing atmospheres. For example, Zhang *et al.*[57] reported the structural evolution and reversible transformation among α-Fe_2O_3, Fe_3O_4, and γ-Fe_2O_3 nanoparticles under reducing and oxidizing conditions. In addition, Jung and Schimpf[58] demonstrated that nanocrystalline γ-Fe_2O_3 can be reduced to Fe_3O_4 via partial reduction of Fe^{3+} to Fe^{2+}. These studies provide literature support for the reversible γ-Fe_2O_3/Fe_3O_4 transformation proposed in this work.

When *n*-butanol is introduced, it reacts with surface oxygen species, releasing electrons that reduce part of the Fe^{3+} to Fe^{2+} in the vacancies. This transforms the material into Fe_3O_4 with a perfect spinel structure, forming a mixed-valence chain (-Fe^{2+}-Fe^{3+}-Fe^{2+}-Fe^{3+}-) and decreasing the resistance[11]. Upon re-exposure to

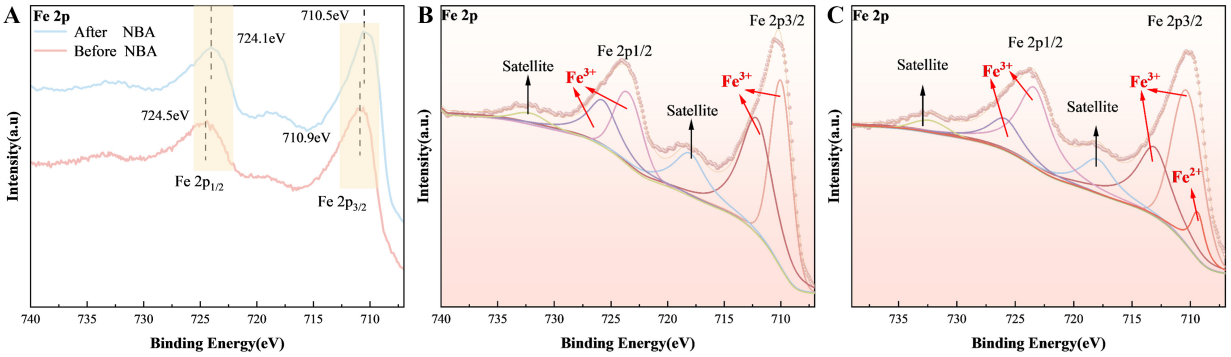

Figure 5. (A) XPS Fe 2p spectra of the 15%-Fe400 sample before and after exposure to *n*-butanol; (B) Deconvoluted XPS spectra and corresponding fitted peaks of the sample before *n*-butanol exposure; (C) XPS peak deconvolution results of the sample after contact with *n*-butanol. All subfigures are original and were plotted using Origin 2024. XPS: X-ray photoelectron spectroscopy.

air, Fe_3O_4 is reoxidized to γ-Fe_2O_3, increasing resistance (as shown in the equations below). As shown in Figure 5A, XPS analysis of the 15%-Fe400 sample before and after exposure to *n*-butanol reveals a reversible redox process on the material surface. The shift of the Fe 2p peaks toward lower binding energies indicates partial reduction of Fe^{3+} to Fe^{2+}, corresponding to a structural transition from γ-Fe_2O_3 to Fe_3O_4[59]. The deconvoluted spectra in Figure 5B confirm that Fe^{3+} is the dominant species in the pristine sample, whereas additional peaks attributed to Fe^{2+} appear after *n*-butanol exposure, as shown in Figure 5C[23]. More importantly, the emergence of Fe^{2+} components after *n*-butanol exposure provides direct evidence of mixed-valence Fe^{2+}/Fe^{3+} states, a characteristic feature of Fe_3O_4. Therefore, the Fe 2p XPS evolution in Figure 5 confirms the surface redox reaction between *n*-butanol and γ-Fe_2O_3 and supports the local γ-Fe_2O_3 Fe_3O_4 transformation during sensing. After re-exposure to air, Fe^{2+} is reoxidized to Fe^{3+}, corresponding to the reverse Fe_3O_4 γ-Fe_2O_3 process and recovery of sensor resistance.

$$C_4H_8OH + 12O^-(ads) \rightarrow 4CO_2 + 5H_2O + 12e^- \quad (6)$$

$$Fe^{3+} + e^- \rightarrow Fe^{2+} \quad (7)$$

$$Fe^{2+} - e^- \rightarrow Fe^{3+} \quad (8)$$

$$\gamma - Fe_2^{3+}O_3^{2-} \leftrightarrows Fe^{2+}O^{2-} \cdot Fe_2^{3+}O_3^{2-} \ (Fe_3O_4, x = 1) \quad (9)$$

From a mechanistic perspective, the gas-sensing behavior of MOF-derived γ-Fe_2O_3 arises from the synergistic interactions among oxygen adsorption-desorption, reversible iron valence transitions, and cation-vacancy migration. In γ-Fe_2O_3, cation vacancies at octahedral sites compensate for the positive charge contributed by Fe^{2+} and part of Fe^{3+}[60]. Under reducing conditions, Fe^{3+} ions are partially reduced to Fe^{2+}, promoting structural conversion toward Fe_3O_4. When re-exposed to air, adsorbed oxygen species capture electrons and oxidize Fe^{2+} back to Fe^{3+}, enabling the reversible γ-Fe_2O_3 Fe_3O_4 transition. Oxygen vacancies play a dual role in this process, acting as both active sites and regulatory centers. They facilitate the formation of reactive oxygen species and dynamically regulate vacancy distribution throughout the adsorption-reaction cycle. These vacancies originate from coordinatively unsaturated metal sites. An increase in their concentration lowers the phase-transition energy barrier and induces local lattice distortion, thereby accelerating structural transformation and resistance modulation while maintaining overall crystal stability[61].

To further enhance oxygen-vacancy concentration, the coordination ratio between H_2BDC and H_3BTC was precisely adjusted during the synthesis of the MIL-100(Fe) precursor. Because H_2BDC exhibits a stronger coordination affinity toward Fe^{3+}, some carboxyl groups in H_3BTC remain uncoordinated, leading to the

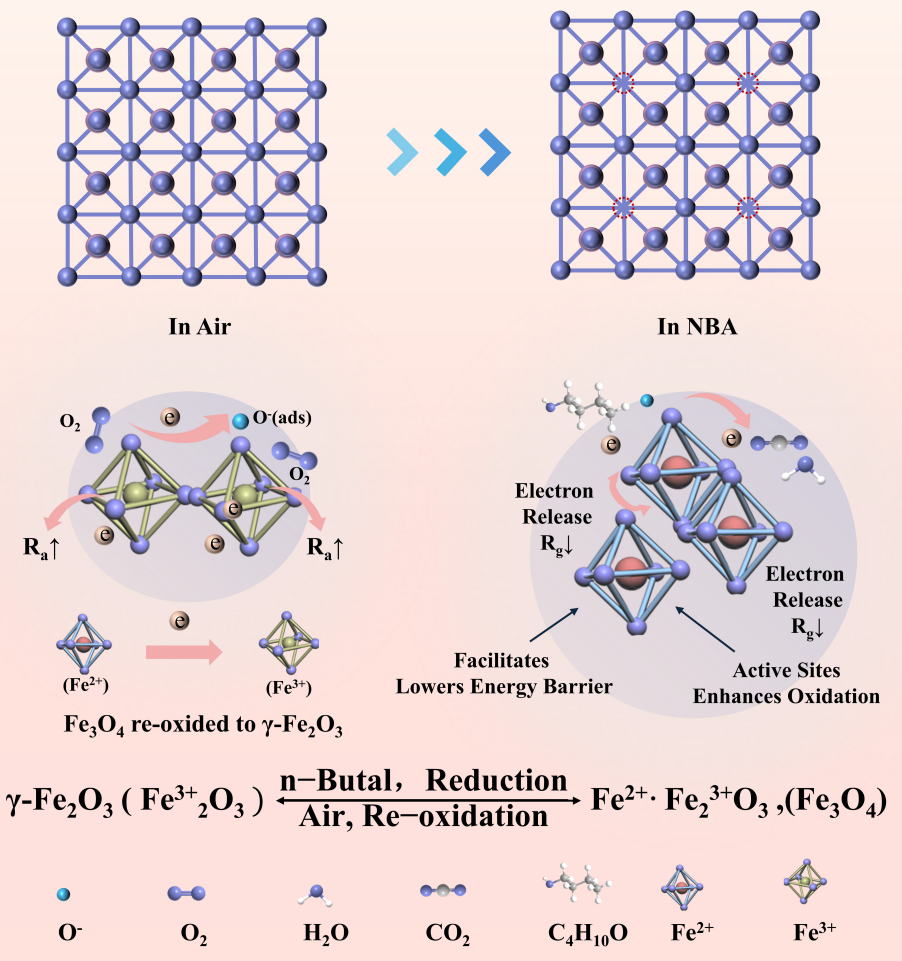

Figure 6. Sensing mechanisms of γ-Fe_2O_3. This figure is original and was prepared using Microsoft PowerPoint.

formation of localized coordination defects[62]. During subsequent heat treatment, these defects were converted into oxygen vacancies, significantly increasing their density and surface reactivity[63]. XPS, Raman, and EPR analyses consistently confirm that the 15%-Fe400 sample exhibits the highest oxygen-vacancy concentration. Therefore, as illustrated in Figure 6, the increased oxygen-vacancy concentration synergistically enhances *n*-butanol sensing through the coupling of surface adsorption-reaction processes with the reversible γ-Fe_2O_3/Fe_3O_4 redox transition. Specifically, the oxygen-vacancy-rich structure introduces local lattice distortion and perturbs the Fe-O coordination environment, as evidenced by broadened Raman signals and modified O 1s XPS components. Such defect-induced distortion weakens local Fe-O bonding and generates electronically unsaturated Fe sites, making Fe^{3+} more susceptible to electron capture during reaction with *n*-butanol. Consequently, Fe^{3+} Fe^{2+} reduction is facilitated, promoting mixed-valence Fe^{2+}/Fe^{3+} formation and lowering the energy barrier for the local γ-Fe_2O_3 Fe_3O_4 transformation. This transition induces a pronounced change in resistance during gas-solid interaction, enabling efficient conversion of chemical signals into electrical responses[64].

In addition to facilitating the phase transition, oxygen vacancies also act as highly active adsorption-reaction sites[65]. They promote oxygen adsorption and activation, accelerate *n*-butanol oxidation, and enhance electron release back to the sensing layer. These released electrons further drive the Fe^{3+}/Fe^{2+} redox process

and reinforce the reversible γ-Fe_2O_3 Fe_3O_4 transformation. Therefore, oxygen vacancies enhance sensing performance through two coupled roles: lowering the phase-transition barrier via local lattice distortion and increasing surface reactivity through abundant adsorption-reaction sites. This clear relationship between oxygen-vacancy-induced lattice distortion, facilitated Fe^{3+}/Fe^{2+} redox conversion, and enhanced surface kinetics further supports the mechanistic model presented in Figure 6.

CONCLUSION

This study aimed to enhance the *n*-butanol-sensing performance of MOF-derived γ-Fe_2O_3 by integrating defect engineering with machine learning-assisted signal correction. The coordinated regulation of precursor structure and heat treatment yielded oxygen-vacancy-enriched γ-Fe_2O_3, which exhibited improved *n*-butanol sensing performance compared with that of unmodified samples. The optimized sensor exhibited improvements in response value, operating temperature, and trace detection capability, while machine learning further improved humidity-related signal correction and multi-gas recognition. Overall, this work demonstrated that combining defect-regulated material design with data-driven calibration provides a promising strategy for developing high-performance, environmentally adaptive gas sensors.

DECLARATIONS

Authors' contributions

Conceptualization: Bo, L. B.; Li, Z. L.; Zheng, X. H.; Liu, Y. F.
Formal analysis: Bo, L. B.; Li, Z. L.
Investigation: Bo, L. B.; Li, Z. L.; Ren, S. Y.; Gu, Z. Q.; Pan, J. W.; Liu, Y. F.
Methodology: Bo, L. B.; Li, Z. L.
Validation: Bo, L. B.; Li, Z. L.; Gu, Z. Q.; Pan, J. W.; Liu, Y. F.
Writing original draft: Bo, L. B.; Li, Z. L.
Funding acquisition: Zheng, X. H.; Liu, Y. F.
Project administration: Zheng, X. H.
Resources: Zheng, X. H.; Liu, Y. F.
Supervision: Zheng, X. H.
Writing - review & editing: Zheng, X. H.
Data curation: Ren, S. Y.

Availability of data and materials

The data supporting the findings of this study are available from the corresponding authors upon reasonable request.

AI and AI-assisted tools statement

During the preparation of this manuscript, the AI tool ChatGPT (GPT-5.5 Thinking, OpenAI; released 2026-4-23) was used solely for language editing. The tool did not influence the study design, data collection, analysis, interpretation, or the scientific content of the work. All authors have carefully reviewed and verified the AI-assisted text and take full responsibility for the accuracy, integrity, and final content of the manuscript.

Financial support and sponsorship

This work is supported by the National Natural Science Foundation of China (NSFC) (62504157, 62275161 and U2141240).

Conflicts of interest

All authors declared that there are no conflicts of interest.

Ethical approval and consent to participate

Not applicable.

Consent for publication

Not applicable.

Supplementary Materials

Supplementary Materials

REFERENCES

1. Bougault, V.; Carlsten, C.; Adami, P. E.; et al. Air quality, respiratory health and performance in athletes: a summary of the IOC consensus subgroup narrative review on 'Acute Respiratory Illness in Athletes'. *Br. J. Sports. Med.* **2025**, *59*, 480-90. DOI
2. Jiang, Y.; Liu, J.; Jiang, W.; Yang, Y.; Yang, S. Current status and prospects of industrial bio-production of n-butanol in China. *Biotechnol. Adv.* **2015**, *33*, 1493-501. DOI
3. Yuan, Z. Y.; Yang, F.; Zhu, H. M.; Meng, F. L.; Ibrahim, M. High-response n-butanol gas sensor based on ZnO/In_2O_3heterostructure. *Rare. Metals.* **2022**, *42*, 198-209. DOI
4. Chen, X.; Liu, T.; Li, Z.; Yin, X. Recent developments in metal oxide semiconductors for n-Butanol detection. *Materials. Today. Che. Mater. Today. Chem.* **2023**, *33*, 101690. DOI
5. Wang, L.; Song, J.; Yu, C. Metal-organic framework-derived metal oxides for resistive gas sensing: a review. *Phys. Chem. Chem. Phys.* **2023**, *25*, 32747-62. DOI
6. Chen, X.; Behboodian, R.; Bagnall, D.; Taheri, M.; Nasiri, N. Metal-organic-frameworks: low temperature gas sensing and air quality monitoring. *Chemosensors* **2021**, *9*, 316. DOI
7. Begi, A. N.; Hussain, S.; Liaqat, M. J.; et al. Unlocking low-concentration NH_3 gas sensing: an innovative MOF-derived In_2O_3/Co_3O_4 nanocomposite approach. *Mater. Sci. Semicond. Process.* **2024**, *181*, 108641. DOI
8. Chu, N.; Wang, Z.; Gu, F. Oxygen vacancies enabled MOF-derived Tb-SnO_2 compound for a high-response, low detection limit, and humidity-tolerant chemiresistive gas sensor of formaldehyde. *ACS. Appl. Electron. Mater.* **2025**, *7*, 3041-54. DOI
9. Ding, Z.; Zhang, F.; Zheng, H.; et al. *In-situ* MOF-derived strategy for fabricating Cu-doped Zn_2SnO_4 based H_2S gas sensors with ultra-low detection limits. *Microchem. J.* **2025**, *218*, 115654. DOI
10. Wang, J.; Qiu, L.; Huang, H.; et al. Prussian blue derived γ-Fe_2O_3 nanocubes grown in situ on Ti_3C_2Tx MXene to construct heterostructure for ultralow-concentration H_2S sensing. *Sensor. Actuat. B-Chem.* **2025**, *442*, 138104. DOI
11. Wang, M.; Hou, T.; Shen, Z.; Zhao, X.; Ji, H. MOF-derived Fe_2O_3: Phase control and effects of phase composition on gas sensing performance. *Sensor. Actuat. B-Chem.* **2019**, *292*, 171-9. DOI
12. Aysha Parveen, R.; Vinoth, E.; Harish, S.; et al. Oxygen vacancies mediated α-MoO_3 nano-ribbons by Cu doping for highly sensitive, selective and rapid detection of hazardous NO_2 for gas sensor application. *Sensor. Actuat. B-Chem.* **2023**, *389*, 133810. DOI
13. Zhang, L.; Xiong, J.; Ding, B.; Fan, C.; Liu, G.; Li, H. Metal-organic framework-derived oxygen-rich vacancies and porous TiO_2 nanotablets for hydrogen detection with high response at room temperature. *Sensor. Actuat. B-Chem.* **2024**, *407*, 135471. DOI
14. Paul, R.; Maity, N.; Das, B.; et al. Controllable oxygen vacancy defect engineering of $BiVO_4$ porous structures for room temperature NH_3 detection. *Chem. Eng. J.* **2025**, *515*, 163814. DOI
15. Li, L.; Diao, Q.; Liu, Z.; et al. Preparation of Co_3O_4 by tunable oxygen defect engineering and its application in acetone gas sensor. *Microchem. J.* **2025**, *212*, 113481. DOI
16. Cai, H.; Luo, H.; Hu, F.; Wang, J.; Zhou, J.; An, D. High-response n-butanol gas sensor based on quasi-Zn-MOFs with tunable surface oxygen vacancies. *J. Alloys. Compd.* **2025**, *1010*, 177274. DOI
17. An, D.; Chen, L.; Liang, Y.; Hou, J.; Chen, J. Defect-containing metal-organic framework materials for sensor applications. *J. Mater. Chem. A.* **2024**, *12*, 38-58. DOI
18. Al-hashem, M.; Akbar, S.; Morris, P. Role of oxygen vacancies in nanostructured metal-oxide gas sensors: a review. *Sensor. Actuat. B-Chem.* **2019**, *301*, 126845. DOI
19. Ji, Y.; Pan, Z.; Ma, T.; Wang, K.; Zhao, X.; Jin, Q. Hierarchical porous spindle-shaped MIL-88B@Fe_2O_3 with core-shelled structure for conductometric trimethylamine detection. *Sensor. Actuat. B-Chem.* **2024**, *417*, 136103. DOI
20. Guo, J.; Jia, H.; Zhang, A.; et al. MIL-100 (Fe) with mix-valence coordinatively unsaturated metal site as Fenton-like catalyst for efficiently removing tetracycline hydrochloride: Boosting Fe(III)/Fe(II) cycle by photoreduction. *Sep. Purif. Technol.* **2021**, *262*, 118334. DOI

21. Wu, Z.; Liu, Y.; Zhang, C.; Zheng, X. Electron sensitization and chemical sensitization of $ZnWO_4/WO_3$ nanorod heterojunctions for high performance triethylamine sensor. *Sensor. Actuat. B-Chem.* **2025**, *424*, 136870. DOI
22. Liu, F.; Li, J.; Li, P.; Shi, J.; Gao, X.; Xu, H. α-Fe_2O_3 derived from metal-organic frameworks as high performance sensing materials for acetone detection. *Sensor. Actuat. B-Chem.* **2024**, *403*, 135147. DOI
23. Guo, J.; Zhang, A.; Pei, Z.; Liu, X.; Xu, B.; Jia, H. Efficient photo-Fenton degradation performance, mechanism, and pathways of tetracycline hydrochloride over missing-linker metal-organic framework with mix-valence coordinatively unsaturated metal sites. *Sep. Purif. Technol.* **2022**, *287*, 120568. DOI
24. Simon, M. A.; Anggraeni, E.; Soetaredjo, F. E.; et al. Hydrothermal synthesize of HF-free MIL-100(Fe) for isoniazid-drug delivery. *Sci. Rep.* **2019**, *9*, 16907. DOI PubMed PMC
25. Zhang, X.; Xu, X.; Fu, Q.; et al. Self-assembled microalgae-photosensitized biohybrids enabling solar-driven directed phosphate conversion form malathion. *Water. Res.* **2026**, *288*, 124787. DOI
26. Kumaravel, S.; Kumaravel, S.; Chandramoorthy, C.; et al. Br-modified nitrogen-rich g-C_3N_5 integrated α-Fe_2O_3 heterostructures for efficient electrocatalytic water splitting and norfloxacin detoxification under LED lighting. *Sep. Purif. Technol.* **2026**, *380*, 135332. DOI
27. Tuček, J.; Machala, L.; Ono, S.; et al. Zeta-Fe_2O_3 - a new stable polymorph in iron(III) oxide family. *Sci. Rep.* **2015**, *5*, 15091. DOI
28. Machala, L.; Tuček, J.; Zbořil, R. Polymorphous transformations of nanometric iron(III) oxide: a review. *Chem. Mater.* **2011**, *23*, 3255-72. DOI
29. Sanap, D.; Avhad, L.; Ghotekar, S.; Gaikwad, N. D. Green synthesis and characterization of mixed-phase Fe_2O_3 nanorods as a novel magnetically recoverable heterogeneous catalyst for Biginelli synthesis. *J. Mol. Struct.* **2023**, *1283*, 135246. DOI
30. Chen, K.; Wu, C. D. Transformation of metal-organic frameworks into stable organic frameworks with inherited skeletons and catalytic properties. *Angew. Chem. Int. Ed.* **2019**, *58*, 8119-23. DOI
31. Wang, Y.; Li, L.; Liang, H.; et al. Superstructure of a metal-organic framework derived from microdroplet flow reaction: an intermediate state of crystallization by particle attachment. *ACS. Nano.* **2019**, *13*, 2901-12. DOI
32. Karuppasamy, K.; Sharma, A.; Vikraman, D.; et al. Room-temperature response of MOF-derived Pd@PdO core shell/γ-Fe_2O_3 microcubes decorated graphitic carbon based ultrasensitive and highly selective H_2 gas sensor. *J. Colloid. Interface. Sci.* **2023**, *652*, 692-704. DOI
33. Huang, Y.; Fan, L.; Liu, Y.; Zheng, X. High-performance MoO_3 nanosheets gas sensors for triethylamine detection: a rapid approach for assessing fish freshness. *Ceram. Int.* **2025**, *51*, 9912-22. DOI
34. Yang, Y.; Liu, Y.; Zheng, X.; Qiao, X. Synthesis of α-Fe_2O_3 nanorod for sensitive and selective detection of the n-butanol. *Solid-State. Electron.* **2024**, *217*, 108934. DOI
35. Ahemad, H. I.; More, M. A.; Hiremath, P.; et al. Green synthesis of lanthanum oxide nanoparticles using *Coleus Barbatus*: annealing effect on gas sensing and antimicrobial efficacy applications. *Small* **2025**, *21*, e05604. DOI
36. Zhao, Z.; Qi, X.; He, Y.; et al. Oxygen vacancy-rich $Fe_2(Mo_3O_4)$ combined with MWCNTs for electrochemical sensors of fentanyl and its analogs. *Microchim. Acta.* **2024**, *191*, 159. DOI
37. Kumar, R.; Al-Dossary, O.; Kumar, G.; Umar, A. Zinc oxide nanostructures for NO_2 gas-sensor applications: a review. *Nano-Micro. Lett.* **2014**, *7*, 97-120. DOI
38. Li, X.; Li, D.; Xu, J.; et al. Calcination-temperature-dependent gas-sensing properties of mesoporous α-Fe_2O_3 nanowires as ethanol sensors. *Solid. State. Sci.* **2017**, *69*, 38-43. DOI
39. Bai, J.; Li, Y.; Liu, Y.; et al. $Au_{39}Rh_{61}$ alloy nanocrystal-decorated $W_{18}O_{49}$ for enhanced detection of *n*-butanol. *ACS. Sens.* **2019**, *4*, 2662-70. DOI
40. Yang, L.; Fu, W.; Wang, Y.; et al. ZnO/LIG nanocomposites to detect acetone gas at room temperature with high sensitivity and low detection limit. *Chem. Eng. J.* **2025**, *519*, 164857. DOI
41. Guo, W.; Li, X.; Gao, X.; Zeng, W.; Wang, X. Designed synthesis of Fe-doped $CoSn(OH)_6$ nanocubes with enhanced N-butyl alcohol gas sensing properties. *Sensor. Actuat. B-Chem.* **2023**, *379*, 133292. DOI
42. Yue, Q.; Liu, T.; Mu, Y.; Chen, X.; Yin, X. Enhanced response for triethylamine detection by $NiCo_2O_4$-In_2O_3 composites gas sensor. *Chem. Eng. J.* **2025**, *509*, 161378. DOI
43. Qu, Y.; Ding, Z.; Lu, X.; et al. Pt-modified hollow tube-like polyaniline-based NH_3 sensor. *J. Hazard. Mater.* **2025**, *485*, 136723. DOI
44. Qu, Y.; Ding, Z.; Yuan, X.; et al. Highly responsive n-butanol gas sensor based on double-shell ZnO hollow microspheres. *Microchem. J.* **2024**, *200*, 110242. DOI
45. Zhou, F.; Mu, Z.; Yuan, Z.; Zhang, R.; Yan, X.; Meng, F. The enhanced n-butanol gas sensing properties based on perovskite-type $ZnSnO_3$ nanoflowers. *Sensor. Actuat. B-Chem.* **2026**, *447*, 138857. DOI

46. Zhao, Z.; Su, Z.; Wu, L. Enhanced n-butanol gas sensors based on ZnO/$CuCo_2O_4$ heterojunction: materials synthesis, sensing performance, and mechanism study. *J. Alloys. Compd.* **2025**, *1030*, 180962. DOI
47. Hao, L.; Li, J.; Wang, X.; et al. Electrospun $FeVO_4$ nanofibers-based gas sensor with high selectivity and fast-response towards n-butanol. *Sensor. Actuat. B-Chem.* **2025**, *433*, 137515. DOI
48. Guo, W.; Shuai, Y.; Liu, X.; et al. A n-butanol gas sensor with enhanced gas sensing performance based on Co-doped $BiVO_4$ polyhedrons. *Sensor. Actuat. B-Chem.* **2022**, *354*, 131221. DOI
49. Pan, H.; Li, Z.; Lou, C.; et al. Anchoring Fe_2O_3 nanosheets on NiO nanoprisms to regulate the electronic properties for improved n-butanol detection. *Sensor. Actuat. B-Chem.* **2022**, *354*, 131223. DOI
50. Li, Y.; Wang, X.; Sun, G.; Cao, J.; Wang, Y. In situ modification of discoid α-Fe_2O_3 nanostructures with Bi_2WO_6 for high performance n-butanol sensor. *Vacuum* **2023**, *216*, 112478. DOI
51. Guo, W.; Jian, L.; Wang, X.; Zeng, W. Hydrothermal synthesis of Ni-doped hydrangea-like Bi_2WO_6 and the enhanced gas sensing property to n-butanol. *Sensor. Actuat. B-Chem.* **2022**, *357*, 131396. DOI
52. Abdullah, A. N.; Kamarudin, K.; Kamarudin, L. M.; et al. Correction model for metal oxide sensor drift caused by ambient temperature and humidity. *Sensors* **2022**, *22*, 3301. DOI PubMed PMC
53. Arroyo, P.; Gómez-Suárez, J.; Suárez, J. I.; Lozano, J. Low-cost air quality measurement system based on electrochemical and PM sensors with cloud connection. *Sensors* **2021**, *21*, 6228. DOI PubMed PMC
54. Ali, S.; Alam, F.; Arif, K. M.; Potgieter, J. Low-cost CO sensor calibration using one dimensional convolutional neural network. *Sensors* **2023**, *23*, 854. DOI PubMed PMC
55. Cava, C. E.; Sun, H.; Huang, S.; Cuniberti, G. Optimized gas sensor array with AI for distinguishing and classifying similar odorants. *IEEE. Sensors. J.* **2026**, *26*, 14595-601. DOI
56. Weyrauch, I.; Hefler, E. L.; Breuch, R.; Kaul, P.; Mathur, S.; Konstantynovski, K. Recent developments in the design of photoactivated metal oxide gas sensors and application of plasmonic nanoparticles in hydrogen-sensing devices. *Physica. Status. Solidi. (a).* **2025**, *223*, e202400633. DOI
57. Zhang, X.; Niu, Y.; Meng, X.; Li, Y.; Zhao, J. Structural evolution and characteristics of the phase transformations between α-Fe_2O_3, Fe_3O_4 and γ-Fe_2O_3 nanoparticles under reducing and oxidizing atmospheres. *CrystEngComm* **2013**, *15*, 8166. DOI
58. Jung, H.; Schimpf, A. M. Photochemical reduction of nanocrystalline maghemite to magnetite. *Nanoscale* **2021**, *13*, 17465-72. DOI
59. Yamashita, T.; Hayes, P. Analysis of XPS spectra of Fe^{2+} and Fe^{3+} ions in oxide materials. *Appl. Surf. Sci.* **2008**, *254*, 2441-9. DOI
60. Qiu, L.; Wu, Z.; Liu, Y.; et al. Mn doping at high-activity octahedral vacancies of γ-Fe_2O_3 for oxygen reduction reaction electrocatalysis in metal-air batteries. *Angew. Chem. Int. Ed.* **2024**, *64*, e202421918. DOI
61. Ji, H.; Zeng, W.; Li, Y. Gas sensing mechanisms of metal oxide semiconductors: a focus review. *Nanoscale* **2019**, *11*, 22664-84. DOI
62. Duan, C.; Yu, Y.; Yang, P.; et al. Engineering New Defects in MIL-100(Fe) via a mixed-ligand approach to effect enhanced volatile organic compound adsorption capacity. *Ind. Eng. Chem. Res.* **2019**, *59*, 774-82. DOI
63. Yu, S.; Dong, J.; Wang, H.; Li, S.; Zhu, H.; Yang, T. Correction: High-performance trimethylamine gas sensors based on defect-engineering MOF-derived ZnO nanoclusters with tunable surface oxygen vacancies. *J. Mater. Chem. A.* **2022**, *10*, 25752. DOI
64. Strapasson, G. B.; Arjona, A. S.; Mcpeak, J. E.; et al. Oxygen vacancy-induced phase transformations of iron-doped titanium oxide nanostructures. *ACS. Nano.* **2025**, *19*, 30986-99. DOI PubMed PMC
65. Zhang, C.; Liu, G.; Geng, X.; Wu, K.; Debliquy, M. Metal oxide semiconductors with highly concentrated oxygen vacancies for gas sensing materials: a review. *Sensor. Actuat. A-Phys.* **2020**, *309*, 112026. DOI